Ag@Pt Core–Shell Nanoparticles for Plasmonic Catalysis

Yinan Fan, Adrien Girard, Michael Walls, Caroline Salzemann, Alexa Courty

To cite this version:

Yinan Fan, Adrien Girard, Michael Walls, Caroline Salzemann, Alexa Courty. Ag@Pt Core–Shell Nanoparticles for Plasmonic Catalysis. ACS Applied Nano Materials, 2023, 6 (2), pp.1193-1202. 10.1021/acsanm.2c04767 . hal-04004084

HAL Id: hal-04004084
https://hal.science/hal-04004084

Submitted on 24 Feb 2023

Ag@Pt Core-Shell Nanoparticles for Plasmonic Catalysis

Yinan Fan[1], Adrien Girard[1], Michael Waals[2], Caroline Salzemann[1]* and Alexa Courty[1]*

1-Sorbonne Université, MONARIS, CNRS-UMR 8233, 4 Place Jussieu, 75005 Paris, France.
2-Laboratoire de Physique des Solides, Université Paris-Sud, 91405 Orsay, France

KEYWORDS: synthesis, seed-mediated growth, core-shell nanoparticles, plasmonic, catalysis

Abstract

Bimetallic nanocatalysts (NCs) composed of two metal elements are a promising way to achieve high catalytic performance, based on so-called synergistic effects. In this context, we have designed bimetallic core-shell nanoparticles (NPs) combining a plasmonic metal Ag as core and a catalytic metal Pt as shell. Ag@Pt core-shell NPs were synthesized via a seed-mediated growth process allowing fine control of the Ag core size and Pt shell thickness. In a first step, Ag seeds (8-13nm) with a narrow size distribution (<10%) were synthesized via chemical reduction by tuning the reaction time, heating ramp and temperature. In the second step, we tuned the Pt shell thickness (from 1 to 6 atomic layers) by adjusting the ratio of Pt precursor to silver seed concentrations. The Pt shell covered all the particles, mostly heterogeneously. The robustness and versatility of the synthesis method was tested and successfully applied to different systems (Ag/Au core and Pd/Pt shell). Subsequently, we studied the impact of size and shell thickness on Ag@Pt optical properties by ultraviolet-visible absorption spectroscopy (UV–Vis) and by discrete dipole approximation (DDA) calculations. Finally, Ag@Pt core shell NPs were demonstrated to be more catalytically active than Ag and Pt NPs of similar sizes through a model reaction of reduction of 4-NP into 4-AP in the presence of $NaBH_4$. These results highlight the synergistic catalytic effect of Ag and Pt species which may be due to the electronic structure of Ag@Pt core-shell NPs, but may also arise from the LSPR excitation of the Ag core. This shows the potential of these particles for applications in plasmonic catalysis

1. Introduction

Noble metallic nanoparticles (NPs) such as gold, silver and copper have been long recognized in both the catalysis and plasmonic communities.[1–4] In particular, it has been shown that light excitation of plasmonic metallic NPs can induce photochemical reactions.[5,6] Various mechanisms are known to be competitively or cooperatively at work during plasmonic catalysis, which are closely related to the excitation of localized surface plasmon resonances (LSPR) – collective oscillations of electrons. The main mechanisms include local amplifications of the LSPR-induced electric field that can modify some properties of neighboring molecules (absorption, Raman diffusion, emission...) but also promote chemical transformations, generation of hot electrons and local heating. [6–8] Compared to conventional thermal-driven catalysis, plasmonic catalysis can significantly reduce the temperature required to achieve the desired catalytic activity and offers thus mild reaction conditions improving the stability and the selectivity of the target products[9,10]. In addition, plasmonic catalysis is also capable of exceeding the equilibrium limit of thermocatalytic reactions[11].

After significant successes in the production of single-component nanomaterials with controlled structure (size and morphology)[12–15], research interest has turned to multi-component nanomaterials, which are defined as a hybrid structure consisting of two or more nanoscale domains with distinct differences in chemical compositions or physical characteristics[16–19]. The appeal of these nanostructures lies in their possible synergistic effect due to the cooperation/interaction between different components or domains at the nanoscale, which often leads to improved performance or properties for a given application[11].

A number of strategies based on wet chemistry methods have been proposed and proven applicable for the synthesis of multicomponent nanostructures with desired properties, among which seed-mediated growth, galvanic replacement and ion exchange methods are capable of producing nanomaterials with heterogeneous properties[20–24].

Traditional metal catalysts such as platinum, rhodium and palladium are widely used in many thermal heterogeneous catalysis processes due to their high reactivity, in particular in the production and storage of hydrogen, CO oxidation, organic compound synthesis and may other. applications[25,26] Compared to thermal catalysis, plasmonic catalysis can offer opportunities for reducing the energy input and increasing the selectivity and catalytic activity. The judicious association of traditional Pt metal with lower-cost plasmonic metals such as Ag in the form of a core-shell Ag@Pt NPs thus offers the possibility to retain of combining the plasmonic properties of Ag with the high catalytic performance of the Pt shell. These NPs therefore have great potential for plasmonic catalysis.

In this article, we report the synthesis of Ag@Pt core-shell NPs with low structural dispersion, controlled core size and shell thickness. The influence on the Pt shell growth of reaction time, heating ramp, temperature, [Pt shell] / [Ag seed] concentration ratio and seed size have all been thoroughly investigated. We show that this synthesis is versatile and robust and can thus be extended to different plasmonic core and catalytic shell materials. The core-shell NPs were fully characterized by scanning and transmission electron microscopy (SEM, TEM, STEM), Electron Energy Loss (EELS), and Energy-dispersive X-ray (EDS) spectroscopies. The plasmonic properties of Ag@Pt NPs were studied in relation to their structural parameters by UV-visible spectroscopy coupled with discrete dipole approximation (DDA) calculations. Finally, the catalytic activity of the Ag@Pt NPs was tested through a model reaction of reduction of 4-NP into 4-AP in the presence of $NaBH_4$.

2. Materials and methods

2.1. Chemical

Commercial reagents were used without further purification, and stored in a glovebox in order to avoid any traces of moisture or air contamination. Silver nitrate dioctyl ether, oleic Acid (90%), chloroform (≥ 99%), $Pt(acac)_2$, $Pd(acac)_2$ and gold (III) chloride trihydrate were purchased from Sigma-Aldrich. Oleylamine (80-90%) was bought from ACROS Organics.

2.2. Synthesis of Ag nanoparticle seeds

The synthesis of Ag NPs (Figure SI.1) was based on the reduction of silver nitrate ($AgNO_3$) in oleylamine (OLA), which served as a solvent, reducing agent and stabilization agent. 1 mmol of $AgNO_3$ was dissolved in 5ml of OLA and held at 30℃ for 35 minutes to ensure its complete dissolution. To avoid light degradation of the $AgNO_3$ precursor, the reaction flask was covered with aluminum foil. The solution turned light yellow, indicating the formation of the Ag-oleylamine complex[27]. The solution was then heated up to a target temperature (120°C, 140°C or 240°C) using a set ramping rate (180, 220 or 450°C/h) in N_2 atmosphere. At 120°C, the color of the solution turned dark brown, indicating the formation of Ag(0). Below this temperature the $(OLA)_n$-Ag complex $^+$ was stable and no reduction occurred. After reaching the reaction temperature, the reaction solution was kept at this temperature for a variable reaction time ($t_{reaction}$) of between 30 and 120 minutes with strong stirring, before cooling to room temperature. The resulting solution was then washed with acetone or ethanol to remove oleylamine and excess by-products. The solution was centrifuged at 5500 rpm for 5 min and the precipitate was dispersed in chloroform ($CHCl_3$). To stabilize the final Ag NPs, 20µL of oleic acid (OA) was then added. In some cases, additional washing processes were performed to further remove excess OLA or to reduce the size distribution via a size selective precipitation process[28].

2.3. Synthesis of Au nanoparticle seeds

Au NPs were synthesized by reduction of gold (III) chloride trihydrate ($HAuCl_4•3\ H_2O$) in OLA at 100°C [27]. 0.025 mmol of gold (III) chloride trihydrate was dissolved in 5 ml of OLA at 30°C for 30min, then the solution was heated to 100°C with a ramping rate of 220°C/h. The solution was kept at this temperature for 20 min. The product was washed with acetone, followed by centrifugation at 5500 rpm for 5 min and dispersion in $CHCl_3$.

2.4. Synthesis of core-shell NPs

The formation of core@shell NPs was achieved by a seeding process. In a test tube, 0.105 µmol L^{-1} of Ag (or Au) NP seeds dispersed in chloroform were dried by nitrogen flow and redispersed in 1.7 ml of dioctyl ether. 300µl of a $Pt(acac)_2$ (or $Pd(acac)_2$) solution in OLA (7mM) was added to the seed solution and the mixture was maintained at a target temperature for a given reaction time in a dry bath. Different temperatures (150°C, 200°C and 250°C) and reaction times (60 min, 90 min and 120 min) were used. After reaction, the mixture was cooled to room temperature. The bimetallic nanoparticles formed were then extracted by washing with ethanol (ethanol/reaction solution volume ratio of 1:2) and centrifugation at 5500 rpm for 5 min. The supernatant was removed and the collected precipitate was redispersed in 1ml of chloroform before adding 20µl of OA.

The shell thickness was controlled by varying the ratio R= [shell precursor]/ [metal seeds]. For Ag@Pt NPs, an initial minimum shell precursor concentration of 7 mmol/L was calculated as necessary to deposit at least one atomic layer of Pt on the surface of the larger 13.3nm Ag seeds at a concentration of $1.05*10^{-4}$ mmol L^{-1}. This corresponds to an R value fixed at $R=6.7*10^4$. For all syntheses, the volume of added $Pt(acac)_2$ solution in OLA was kept constant while the concentration was adjusted from 7 mmol/L to 110 mmol/L, corresponding to a ratio variation by a factor of 16. Similarly, for Ag@Pd and Au@Pt NPs, different Pd(acac)$_2$ or Pt(acac)$_2$ concentrations were also used to get different Pt or Pd shell thicknesses.

2.5. Structural characterizations and composition

TEM images were obtained with a JEOL JEM1011 100 kV. *The samples for TEM imaging* were prepared by putting droplets of a dilute solution on a carbon-coated copper grid.

EDS was carried out in a JEOL-JSM-5510LV SEM operating at 20KV. Each sample was washed twice to remove more of the excess of ligands which have a large negative impact on the result of EDS (and EELS). The samples with high concentration were deposited on a conductive adhesive (carbon tape usually used to fix to the solid substrate) instead of the usual silicon substrate because of the close position of Si and Pt peaks in the EDS measurements. It should be noted that for a variation in composition between different positions on the sample of less than 3%, it is reasonable to assume that the sample is homogeneous.

STEM images were taken using a high-angle annular dark field (HAADF) detector in a Nion Ultrastem 200 Cs-corrected microscope operating at 100kV with a probe size of about 0.07 nm. The probe convergence and HAADF detector minimum collection semi-angles were 35 and 75mrad respectively, meaning that HAADF images were dominated by Z-contrast, although some diffraction contrast is possible.
EELS Elemental maps were obtained using electron energy-loss spectroscopy in the spectrum-image (SI) collection mode using the Ag M- and Pt M-edges.

UV-Visible spectroscopies. UV-visible absorption spectra in the range 300nm to 700nm were acquired from all samples with a VARIAN Cary 5000 UV-Vis-NIR spectrometer. QS UV-Vis cells with a length l=1mm were used to measure the NPs' optical response. The concentration of NP seeds in chloroform solution is determined using the Beer's Law formula: $A_{310nm}=l\ \varepsilon\ C_M$ (1) where, A_{310nm} is the UV-visible absorption value of the solution at 310 nm, ε is the molar extinction factor of the metal M and is equal respectively to 2973 and 1200 $cm^{-1}LMol^{-1}$ for M=Ag and Pt; and C_M is the total atomic concentration after synthesis. The NP concentration can be deduced by: $C_{NPS}(mol\ L^{-1}) = \frac{C_M(mol\ L^{-1})\times V_{molaire,M}}{\frac{4}{3}\pi\left(\frac{D_{core}}{2}\right)^3\times Na}$ (2)

Discrete-Dipole Approximation (DDA). The absorption spectra are compared to those calculated using the discrete dipole approximation (DDA) method, which is a flexible and powerful method widely used to simulate the scattering and absorption by nanometer-sized objects of different geometries and dielectric properties. Its principle and accuracy are well described in previous articles [27,29,30]. Here, the extinction spectra of Ag and Ag@Pt NPs are calculated using the free software DDSCAT 7.3 written by Draine and Flatau[31] as well as the dielectric functions of bulk Ag and Pt taken from Palik's handbook [32]. The refractive index of the surrounding medium is fixed at the value n = 1.44, which corresponds to that of the dispersion solvent, i.e. chloroform.

2. Results and discussion

2.1. Synthesis of Ag@Pt core-shell nanoparticles

The physicochemical properties of silver and platinum, including their reduction potentials are very different.[33] Hence if both precursors coexist initially in the chemical media they can be successively reduced respective to their redox potential to form core-shell structures.[34,35] However, considering that platinum has higher redox potential, higher cohesive energy and higher surface free energy than silver, a catalytic platinum core and a plasmonic silver shell is expected.[19,35] In this context, to achieve the formation of the desired plasmonic-core@catalytic-shell bimetallic structures and prevent any alloying, it is necessary to carry out a two-step successive reduction of the metals to selectively deposit the platinum at the silver surface.[21,33]

For this purpose, we have developed a versatile and robust synthesis process in two-steps: i) formation of silver NP seeds with a low structural dispersion (size, shape, crystallinity) ii) growth of the platinum shell on these seeds by heterogeneous reduction and nucleation at their surface. From this synthesis process, both core size and shell thickness can be controlled independently to obtain different $\text{Ag-core}_{\text{size}}$@$\text{Pt-shell}_{\text{thickness}}$ combinations (Figure 1).

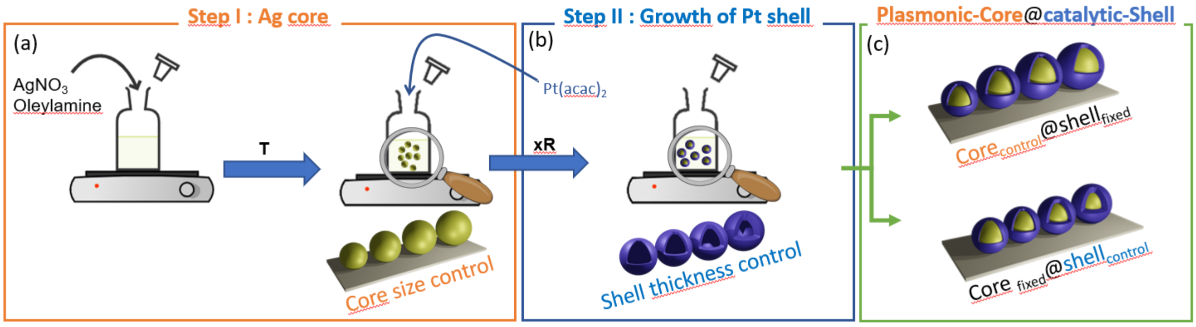

Figure 1: *Synthesis of plasmonic-core@catalytic-shell nanoparticles in a two-step seeding process a) Ag core synthesis and b) platinum shell growth. Core size and platinum shell thickness are controlled independently. T is the temperature and* $xR = x[Pt(acac)_2]/[Ag\ seeds]$ *ratio*

Synthesis of Ag seeds. The formation of the Ag seed nanoparticles is performed via controlled-temperature synthesis as described in the experimental section (Figure SI.1). Various parameters were explored in order to have a robust synthesis method leading to NPs characterized by low structural dispersion in size, shape and crystallinity. In particular, the effect of the ramping rate, of the heating temperature and of the reaction time ($t_{reaction}$) were studied (Figure SI.1). Results of the ramping rate and the reaction time are detailed in the supporting information (SI.3 and SI.4 sections with figures). Even though no average size difference is observed by changing these parameters, they have a clear influence on the size dispersion. Specially, higher ramping rate and a reaction time of 60 minutes constitute the optimum to obtain uniform NPs polydispersity of 8%.

Figure 2 shows TEM images of silver NPs obtained after 60 minutes of reaction at different heating temperatures: 120°C, 140°C and 240°C with a fast-ramping rate of 450°C/h. The ramping times necessary to reach the target temperatures were 11 min., 16 min. and 36 min. respectively. This means that the total time was 71, 76 and 96 min. (Figure SI.5.I). As previously, the TEM images show polycrystalline spherical NPs. The size distributions (Figure SI.5.II) highlight an increase in the average NP size from 8.4 ± 0.7 nm to 10.5 ± 0.9 nm and 13.3 ± 1.3 nm for an increase in reaction temperature from 120°C to 140°C and 240°C respectively, with a size dispersion of less than 9% in all cases. As seen previously, the low polydispersity obtained after one hour of reaction can be explained by the high ramping rate which induces burst nucleation associated with probable digestive ripening during the first hour

(Figure SI.4.II). Since the ramping rate is fixed and reduction is observed as early at 120°C, we can reasonably assume that reduction and nucleation occur in a similar way for all samples. Diffusion-controlled growth in the Ostwald ripening process is known to be influenced by temperature.[36] This is due to changes in interfacial energy, growth rate coefficients, and solubility with temperature. Therefore, as the diffusion and growth rate coefficients increase with increasing temperature, larger NP sizes are obtained at higher reaction temperatures. This is consistent with our observations (Figure 2) as well with those of Prasad et. al.[36,37]

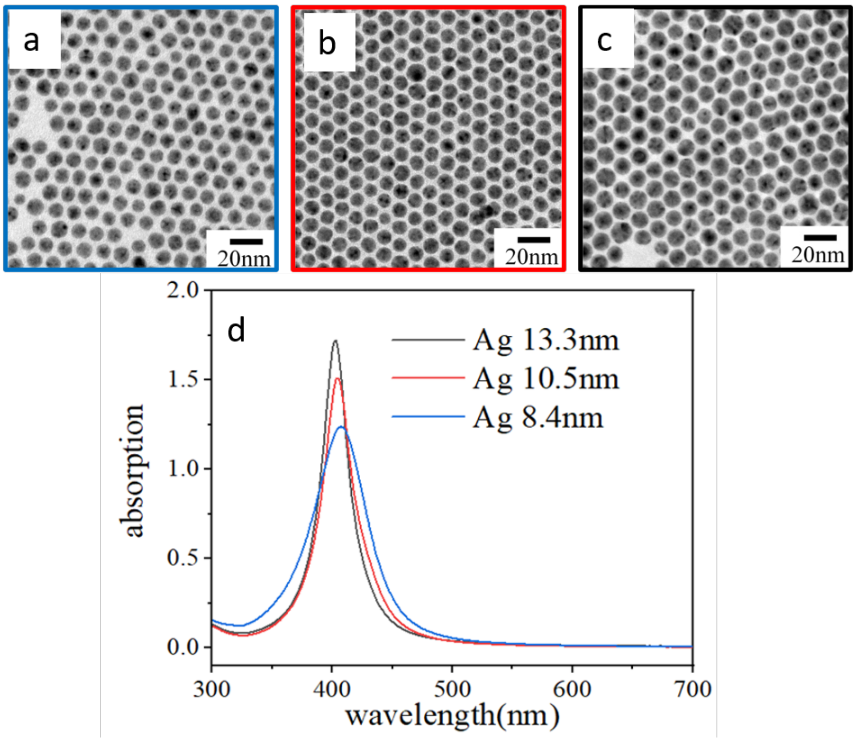

Figure 2. *TEM images of Ag NPs obtained by fast ramping (450°C/h) after one hour of reaction at different reaction temperatures, (a) 120°C, (b) 140°C, (c) 240°C and (d) the corresponding UV-visible spectra.*

Figure 2.d shows the different absorption spectra obtained for the three different NP sizes. It is worth noting that the maximum absorption peak position of Ag NPs is dependent on their size. As we can see, this peak shifts from 410 nm to 409 nm and to 406 nm, when the size of the NPs increases from 8.4nm, to 10.5nm and then to 13.3nm. This observation may seem surprising because it is in disagreement with the effect of the size of the NPs according to the Mie theory[38]. However, similar results were already reported[39]. In fact, a blue-shift then red-shift switch is observed when increasing the size of the nanoparticles. The absorption band red

shifts when the Ag NP size increases from 12.5 nm to 20 nm, but it blue shifts when the Ag NP size increases from 2 nm to 12.5 nm, in chloroform. The position of the LSPR peak in small NPs results from a balance between two counteracting quantum size effects, namely the effects induced by the electron spill-out yielding a red shift with decreasing size and a reduced screening of d surface electrons yielding a blue shift. The inversion behaviour of LSPR at the turning point around 12nm has been reported previously and was interpreted by a decrease in conductivity in the outer metallic layer compared to the conductivity of the inner Ag atoms due to chemical interactions, in particular with the presence of a capping agent. [39] However, this anomalous behaviour has been revisited in the light of more recent works based on correlated STEM-EELS and optical experiments, that pushed the accessible size range below 10nm. In addition to the known LSPR red-shift effect due to refractive index, the theoretical and experimental results showed that embedding NPs in an environment also alters the relative weight of the two-counteracting size-dependent LSPR shifts, yielding similar trend: a blueshift and red-shift upon decreasing the size of silica embedded Ag NPs.[40] In chemically-stabilized NPs as in our case, the situation is seemingly different due to the electronic structure of the metal core being altered by the localized bonds with ligand and the liquid environment as compared to a solid silica matrix, and it is not surprising that contradictory trends have appeared in the literature over the years due to the sensitivity of this detailed balance upon solvent, surface sate of the NPs, nature of metal-ligand interaction, nature of interface (gas, solid, liquid) and surface coverage of capping ligands.[40] Our result indicates that in our conditions the balance is slightly tilted toward a larger contribution of the electronic spill-out yielding a redshift of the LSPR upon decreasing the NPs size below 12 nm, which may be supported by a decreased conductivity of the outer metallic layer.

Synthesis of Ag@Pt NPs. The Pt shell was grown at the surface of the Ag NPs seeds by adding 300µL of a solution of $Pt(acac)_2$ salt solubilized in OLA in a single step to 1.7mL of a solution of silver NPs ($9x10^{-8}$ mol L^{-1}) dispersed in diocthylether. The mixed solution was then kept at a fixed temperature for one hour. Reduction of the $Pt(acac)_2$ salt was performed in the presence of the spherical Ag NPs and nucleation occurred directly on the silver surface, thereby inducing the formation of a platinum shell around the silver core.

It was observed that a minimal temperature of 200°C is necessary to induce the reduction of platinum (Figure SI.6); for lower temperatures no platinum is detected. At 200°C, the proportions of platinum and silver determined by EDS are constant (less than 3% variation) over the whole sample, which confirms the formation of bimetallic Ag/Pt NPs, excluding the co-existence of two distinct populations of pure Ag and pure Pt. A higher temperature or a longer reaction time have no influence on the composition of the NPs (Figure SI.7). The corresponding absorption spectra clearly show a strong damping and broadening of the plasmon peak for bimetallic NPs compared to pure Ag, indicating that the silver environment has changed.

The characterization of the core-shell structure of the bimetallic NPs is not obvious using conventional TEM because of the lack of contrast between Ag core and Pt shell. To circumvent this problem and have no ambiguity on the structure, HAADF and EELS measurements were performed on different bimetallic samples, the EELS being used to make elemental maps (Figures 3 a and b). The Ag@Pt core-shell structure was confirmed with the silver core indicated in yellow and the platinum shell in blue (Figure 3b). The platinum shell appeared inhomogeneously distributed and discontinuous across the Ag NP surface. Furthermore, we observed that a thin atomic layer of silver was deposited on the platinum shell of some NCs in a discontinuous way (see arrow on Figure 3b). This atomic outer yellow layer can be explained based on a galvanic replacement mechanism, which consists in the oxidation of the silver core (having the lower redox potential) by the Pt ions (having the higher redox potential)[41], in competition with the direct reduction of Pt ions by OLA and subsequent reduction of silver ions by OLA. The galvanic process is not predominant in our synthesis method, probably due to a lowering of the redox potential of platinum following its complexation with OLA (formation of $Pt(OLA)_4(Acac)_2$).[42,43] The reduction rate of the precursor thus becomes higher than the rate of the galvanic reaction and Ag@Pt NPs are formed by the deposition of Pt(0) on silver NPs before Pt^{2+} can react with Ag seeds.

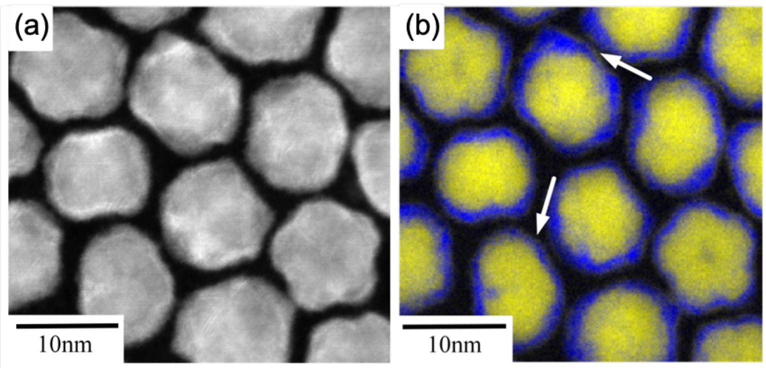

Figure 3. *(a) Typical HAADF-STEM dark field image of AgPt bimetallic NPs (b) corresponding EELS mapping with Ag core (yellow) and Pt shell (blue) confirming the formation of the core-shell structure.*

EDS measurements coupled with SEM were performed in order to determine the global composition of the NPs. Measurements of the diameters of the silver core (D_{core}) and of the core-shell nanoparticles ($D_{core-shell}$) determined from the TEM Images (Figure SI.8 and section SI.8.II) also allowed us to determine the composition of the NPs with a very good agreement with the EDS measurements.

The next step was the preparation of different $Ag_{size}@Pt_{thick}$ core-shell nanoparticles with different core sizes and shell thicknesses using a fixed concentration of Ag NP seeds ($9x10^{-8}$M) but varying the concentration of $Pt(acac)_2$ from 7 mmol L^{-1} to 110 mmol L^{-1}, resulting in a [Pt precursor]/ [Ag seed] ratio equal to 1R, 2R, 4R, 6R, 8R or 16R (see section I.3).

Figure 7 shows typical TEM images of bimetallic core-shell NPs obtained from an Ag core size of 8.4 nm (Figure 4a) with different Pt shell thicknesses. The Pt content has been determined by both TEM and EDS (Table SI.9.I) and a corresponding average shell thickness has been estimated. For the minimum Pt concentration corresponding to a ratio of 1R, Ag@Pt NPs keep the spherical shape of the original Ag seeds (Figure 4a). The average diameter of these NPs is 9.0 nm from which we can deduce a thickness of Pt shell of 0.4 nm (about1 Pt atomic layer). Multiplying R by 2, the Pt shell of Ag@Pt NPs starts to become inhomogeneous (Figure 4b), meanwhile the Pt shell thickness slightly increases to 0.85 nm (around 3 Pt layers). When the [Pt precursor]/ [Ag seed] ratio is increased to 4R, 8R and 16R, the Pt shell thickness increases to 1.1 nm (about 4 Pt layers), 1.6 nm (about 6 Pt layers) and 2.0 nm (about 8 Pt layers), respectively (Figure 4c-d). By increasing the platinum content from 2R (Figure 4b) to 8R (Figure 4d), the NCs' surfaces become more and more irregular. At the highest content corresponding to 16R (Figure SI.9), most of the NCs have a very bumpy surface. The evolution from spherical NPs toward irregular morphology with the increase in the [Pt precursor]/ [Ag seeds] ratio can be explained by the different deposition/diffusion processes during the reactions at different Pt content. From a general point of view, the shell formation occurs by Pt atom deposition on sites that have the highest surface energy followed by diffusion to a site with a lower surface energy. In the literature three well-known growth modes for the shell have been described in the past (i) Frank−van der Merwe (FM): the atomic growth occurs layer by layer; (ii) Volmer-Weber (VW): the atoms form 3-D islands on the seed surface; (iii) Stranski−Krstanov (SK): the atoms are first assembled in Frank−van der Merwe mode, but growth then switches to Volmer−Weber mode.[44] The small lattice mismatch between Ag and Pt (4.1%) and their identical crystalline structures should favour FM growth at least at the beginning or for low Pt content. Conversely, their strong difference in bulk cohesive energy and surface energy disfavours the FM mode to the benefit of the VW mode. As the deposition of Pt was carried out at relatively high temperature, 200°C, it is expected that Pt diffusion should be promoted. At low Pt concentration, considering the high temperature and the low surface energy of silver, Pt atoms should diffuse on the Ag surface relatively easily. However for higher Pt content, as soon as the Ag surface is covered by a Pt shell, this serves as new nucleation centre where Pt atoms stick to form heterogeneous growth due to Pt's higher dissociation energy compared to Ag, limiting the diffusion[44]. We can then assume that a mixed growth mode combining FM and VW modes (SK mode) is the most likely at higher Pt content, explaining the bumpy morphology. In the STEM-HAADF images, the bumpy surface is confirmed for high platinum contents (Figure 3a).

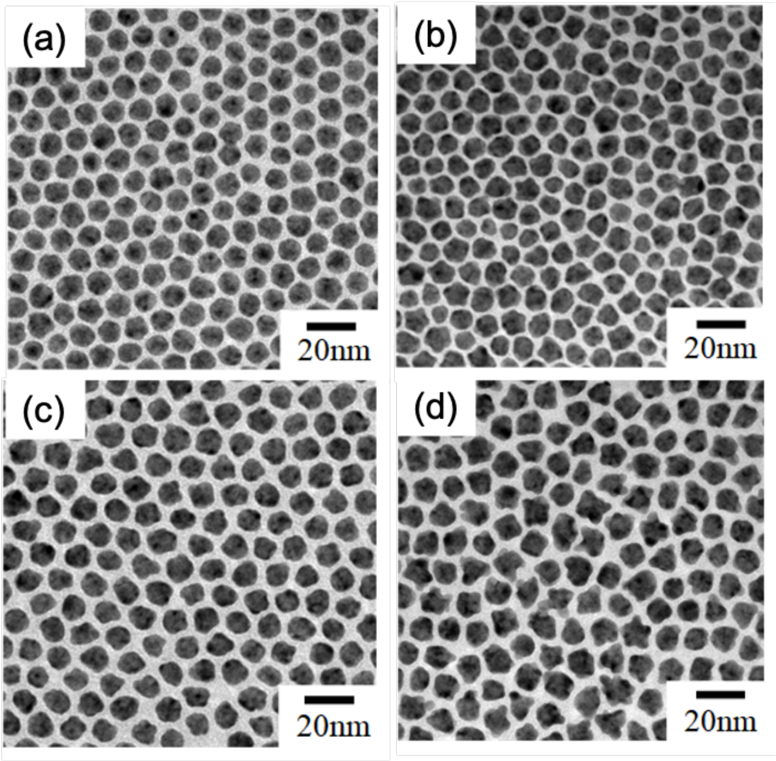

Figure 4. *Representative TEM images of* $Ag_{8.4nm}$*@Pt NPs synthesized for different [Pt precursor]/ [Ag seed] ratio equal to (a) 1R, (b) 2R, (c) 4R, (d) 8R*

Using the same synthesis process as previously described, Ag@Pt core-shell NPs with tunable Pt thickness have been obtained from the 10.5nm (Figure 2b) and 13.3nm (Figure 2c) Ag NPs. The TEM images and the corresponding size dispersion are reported in the supporting information (Figures SI.10. I and SI.10. II). The evolution of Pt shell thickness for different [Pt precursor]/ [Ag seed] ratio and Ag core size is summarized in Table SI.11.

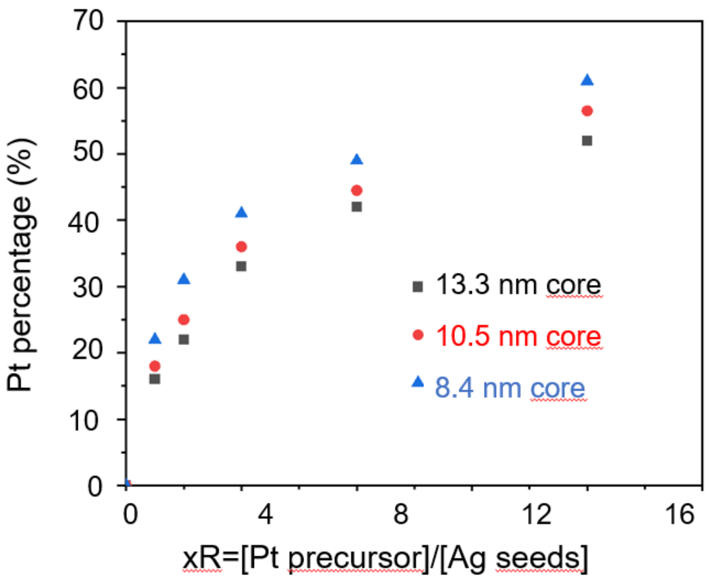

Figure 5. *Evolution of the Pt shell thickness of Ag@Pt NPs for different [Pt precursor]/ [Ag seeds] ratio and Ag core size*

The Pt atomic percentage increases with the increase in [Pt precursor]/ [Ag seeds] ratio, regardless of the core size (Figure 5). However, for a fixed ratio, the atomic percentage of Pt is always larger for the smaller core size. This is not surprising. Indeed, as we always use the same concentration of Ag seeds whatever the core size, for smaller Ag NPs, the total NP surface is lower compared to larger sizes. Hence, for a given [Pt precursor]/ [Ag seeds] ratio, the ratio of platinum to the available Ag surface increases when the core size decreases. This explains the thicker shell of platinum on smaller seeds. In addition, as discussed previously, the platinum initially deposits on the silver surface and can diffuse relatively easily. As soon as the silver surface is covered by platinum, further growth occurs by heterogeneous nucleation of platinum on the formed platinum shell. The diffusion is less efficient due to the strong cohesion energy and more bumpy shells are then obtained.

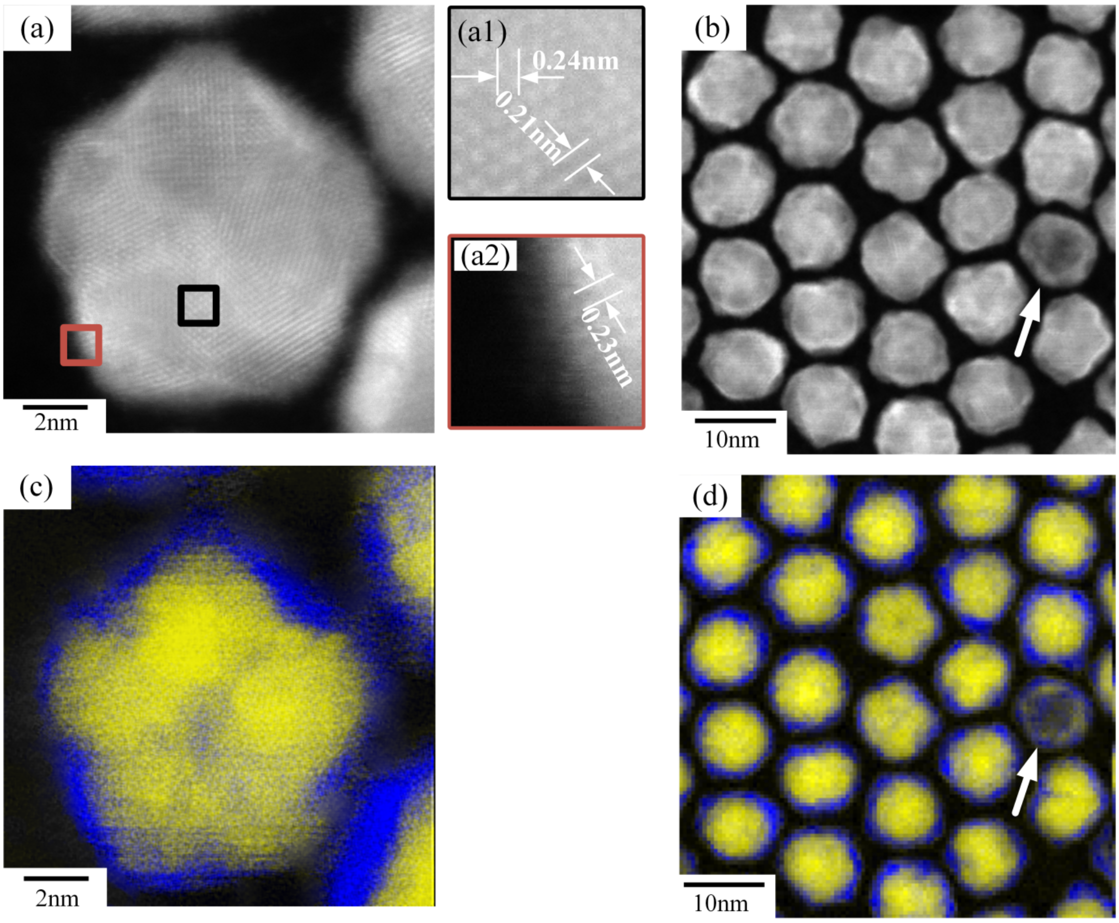

Figure 6. *Electron microscopy characterization of Ag@Pt core shell NPs with 10.5nm core and 4 Pt layers. (a), (a$_1$), (a$_2$) and (b) Typical HAADF-STEM dark field images of NPs, (c) and (d) corresponding EELS mapping (in blue Pt and in yellow Ag).*

Figures 6a and b show representative STEM-HAADF images of $Ag_{10.5nm}$ @$Pt_{4\ atomic\ layers}$ core-shell NPs. The Pt shell seems to grow directly on the surface of Ag NPs, since non clear discontinuity was observed between the lattices. High magnifications in Figures $6a_1$ and $6a_2$ shows the lattice fringes of the Ag core and Pt shell respectively. The two lattice fringes with d-spacings of 0.21nm and 0.24 nm can be attributed respectively to *(200)* and *(111)* crystalline planes of Ag (Figure 6a1). The d-spacing of 0.23 nm is attributed to the *(111)* crystalline plane of Pt (Figure 6a2)[17,45]. The corresponding EELS maps show the distribution of Ag and Pt in the nanoparticle (Figure 9c-d). They confirm the formation of core-shell NPs with an Ag core (yellow) and a more or less continuous Pt shell (blue).

Moreover, we observe some hollow structures in Figure 6d, constituting about 3%-4% of the total probed particles and many Ag@Pt NPs are coated with a very thin Ag layer as observed previously for $Ag_{8.4nm}$@$Pt_{4atomiclayer}$ NPs. The outer thin Ag layer can be formed through galvanic replacement (GR) arising from the oxidation of the metal core ((lower redox potential) by the metallic salt (higher redox potential)[41]. The hollow NPs can thus be the result of the formation and coalescence of voids due to the Kirkendall effect (KE) coupled with GR[46].

Stability of Ag@Pt core-shell NPs. In the targeted purpose of using the core-shell nanoparticles for catalytic application, we must ensure that they do not change over time. The combination of the low surface energy of silver and the high dissociation energy of platinum indeed makes the Ag@Pt systems thermodynamically unfavourable. An evolution toward nanoalloys such as AgPt@Ag or in a best case, Ag@PtAg cannot be excluded. A study of their stability was thus performed. The NP solutions were always stored in a glove box under nitrogen atmosphere. We have studied their structural evolution with time. Two samples were tested: (i) a fresh sample (deposition of a colloidal solution synthesized 2 days before and left in the glove box) and (ii) an old sample (deposition of a colloidal solution synthesized 11 days before and left in the glove box). Both samples show a few hollow structures (Figure SI.12). The percentage of hollow structures increases very slightly from 3-4% to 4-5% with aging. This increase is not significant. These hollow structures are thus formed during the synthesis process and are stable in time. The GR and KE reaction between Ag seeds and Pt^{2+} ions appear thus to weakly interfere with the growth of Pt on Ag seeds, resulting in a small amount of Ag/Pt alloy nanoparticles with hollow interiors instead of core-shell structures.16 In the case of core-shell structures, we can also note that the outer thin Ag shell thickness does not increase with time, confirming its formation during the synthesis.

2.2 Optical properties of Ag@Pt NPs.

Plasmonic catalysis applications rely on matching the light wavelength to the LSPR. We have characterized the optical properties of the synthesized Ag@Pt NPs as a function of core size and shell thickness. Ag NPs are known to have a well-defined Localized Surface Plasmon Resonance (LSPR) band in the visible range. Figure 7a shows a series of experimental spectra collected from monometallic $Ag_{8.4nm}$NPs and bimetallic core-shell $Ag_{8.4nm}$@Pt NPs with different Pt thickness. $Ag_{8.4nm}$ NPs exhibit an LSPR band at around 410nm as expected[47]. The spectra were recorded from colloidal solutions at room temperature with a fixed concentration of $2*10^{-8}$ mol L^{-1}. Moreover, the intensity of the Ag plasmon band decreased with the increase in the surface coverage by Pt atoms. The LSPR band maximum also shifts progressively to the blue (Table SI.13). For a Pt thickness of 1.6 nm (around 6 atomic layers) the LSPR is completely damped and not visible in the UV-Vis spectra. It should be noted that the Pt shell should therefore not exceed a thickness of about 1 nm (i.e. 4 atomic layers) in order to not overdamp the LSPR of the Ag core, which is necessary for plasmonic catalysis applications.

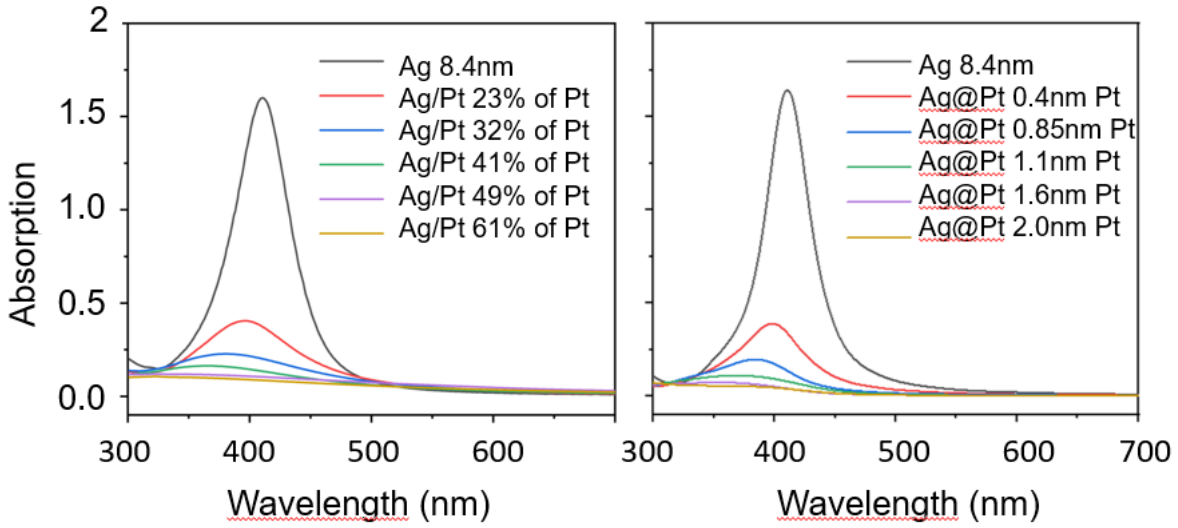

***Figure** 7: (a) Experimental and (b) DDA calculated absorption spectra of core-shell Ag@Pt NPs with various shell thicknesses as indicated in both panels*

To gain deeper insights into the relationship between the SPR bands and the shell thickness, DDA calculations were carried out to simulate the absorption spectra of $Ag_{8.4nm}$ and $Ag_{8.4nm}$ @Pt NPs. In these calculations, the refractive index of the surrounding medium is set to 1.4 to simulate the chloroform used as the solvent. The dielectric functions of bulk Ag and Pt were taken from Palik's handbook.[32] The calculated spectra obtained for different Pt shell thicknesses are plotted in figure 7b and are consistent with the general trend observed in the experimental spectra. They show also a blue shift and damping of the SPR band when Pt shell thickness increases, in good agreement with experimental absorbance spectra (Table SI.13). We can note a broadening of the SPR band in the experimental spectra compared to the calculated spectra, which can be attributed to the size distribution of the NPs which is not taken into account in the calculations. These results confirm the core-shell structure of the NPs.

2.3 Extension to other core and shell materials

The synthesis method of Ag@Pt core-shell NPs that we developed in this work is easily transposable to other bimetallic systems and yields core-shell NPs while keeping a narrow size dispersion and homogeneous shape. We have tested the robustness of our synthesis by replacing i) the Pt shell by a Pd shell and ii) the Ag core by an Au core.

Synthesis of Ag@Pd NPs. Ag NPs 13.3 nm in diameter coated by oleylamine are selected as seeds and $Pd(acac)_2$ was used as the source of Pd. Different [Pd precursor]/ [Ag seed] ratios (1R or 2R) were prepared by changing the $Pd(acac)_2$ concentrations to get different Pd shell thicknesses as realized previously for Ag@Pt NPs. The Ag@Pd NPs were synthesized by heating the solution to 200°C for 1h. The final solution was washed in ethanol followed by centrifugation during 5 min at 5500 rpm and the precipitated particles were then redispersed in chloroform. Typical TEM images of Ag@Pd NPs obtained for the two different [Pd precursor]/ [Ag seed] ratios (1R and 2R) are shown in Figure SI.14. The NPs present quasi-spherical shapes with a narrow size distribution for both ratios. The average Pd shell thicknesses deduced from EDS measurement is in agreement with TEM calculations (see Table SI.14). It increases from 0.3 to 0.5 nm when increasing the [Pd precursor]/ [Ag seeds] ratio from 1R to 2R. A series of spectra collected for monometallic $Ag_{13.3nm}$ NPs and bimetallic core-shell $Ag_{13.3nm}$@Pd NPs with different Pd thickness is presented in Figure SI.14. $Ag_{13.3nm}$ NPs exhibit an SPR band at around 406nm. Moreover, the intensity of the Ag plasmon band decreases with the increase in the surface coverage by Pd atoms. The SPR band maximum also shifts progressively to the blue. This confirms the core-shell structure of the NPs.[27]

Synthesis of Au@Pt NPs. For the synthesis of the core-shell Au@Pt NPs, we used the $Au_{10.4nm}$ NPs as seeds and the $Pt(acac)_2$ precursor. Different [Pt precursor] / [Au seed] ratios (R,2R,4R and 8R) were tested. The reaction was performed at 200°C for 1 h and followed by cooling to room temperature. The solution was precipitated out using ethanol (ethanol /reaction solution volume ratio of 1:2) and centrifuged at 5500 rpm for 5 min. The precipitate was then re-dispersed in chloroform.

For a [Pt precursor] / [Au seed] ratio equal to 1R, Au@Pt NPs with 0.3nm Pt shell are obtained, and their shape remains quasi-spherical as for the initial Au seeds (Figure SI.15 and Table SI.15). As previously observed for others core-shell, when increasing R to 2R and then 8R, the Au @Pt NPs become bumpy, the Pt shell thickness increases progressively from 0.6 nm to 1.2 nm according to the TEM images. The Pt shell thickness is deduced as previously from the composition determined by EDS. The efficiency of Pt overgrowth on Au is thus similar to that on Ag, which can be explained by a similar lattice mismatch for both metals with Pt (around 4.1 %).[48]

2.4 Catalytic activity of Ag@Pt NPs

The catalytic activity of Ag@Pt core-shell NPs was studied through a model reaction of reduction of 4-nitrophenol (4-NP) in 4-aminophenol (4-AP) by sodium borohydride ($NaBH_4$) in aqueous phase. This reaction is indeed reported as a model reaction for investigating the catalytic properties of nanoparticles made of silver, gold, palladium etc.[49–51] The reaction kinetic is easily followed by UV-vis spectroscopy during the colour changes associated with the conversion of 4-NP to 4-AP. In Figure SIX, we can observe a typical example of the trend of the absorption bands related to the consumption of 4-NP and the formation of 4-AP during the chemical reduction of the nitro functional group. In the absence of the catalysts, no reaction was observed at reasonable times.

This model reaction takes place in the aqueous phase, whereas all the NPs synthesized in this work are dispersed in an organic solvent such as chloroform. These NPs are therefore coated with hydrophobic ligands such as OLA associated to a very small amount of OA (see SI.16). Thus, to use these NPs, it is necessary to transfer them into water. For this purpose, the organic ligands were replaced by hydrophilic ligands. We chose a shorter charged ligand, Mercaptosuccinic acid (MSA), to allow transfer of the NPs into water and to promote adsorption of reagents onto the free surface of the NPs for catalysis. MSA has a mercaptan function (HS) which gives it a stronger affinity for metallic NPs than OLA, which promotes ligand exchange.[52,53] The ligand exchange procedure used was adapted from the literature and is described in the supporting information.[54] It works for all the NPs synthesised in this work. EDS analysis was performed to confirm the ligand exchange (see Table SI.16.1).

The catalytic activity of Ag@Pt NPs was compared with that of the monometallic NPs (Ag and Pt). The synthesis process of Pt NPs adapted from that used for Ag NPs and described in details in supporting information, allowed us to obtain NPs with a mean diameter of 9.7 ± 0.5 nm. Ag and Ag@Pt NPs with a core size of 8.4 nm close to that of Pt were thus selected and the thickness of the Pt shell was set at 1.1 nm (around 4 Pt atomic layers). This Pt shell thickness is the limit for observing Ag LSPR. The concentration of the NP solution was calculated from UV-Vis spectra (see experimental section) and then adjusted to have the same total surface area regardless of the NPs. The temperature was fixed at 20°C.

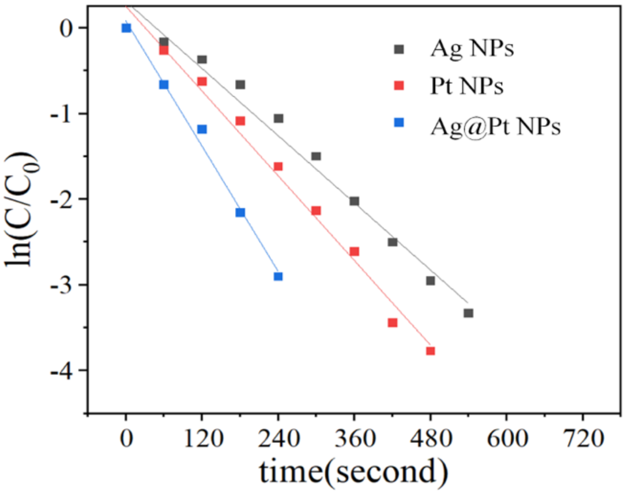

Figure 8. *Plots of ln(C/C$_0$) versus reaction time for the conversion of 4-NP with the use of Ag@Pt, Ag and Pt NPs as nanocatalysts.*

The 4-NP reduction reaction can be treated as a first order reaction in the presence of $NaBH_4$ excess, so ln(C/C$_0$) where C=[4-NP]t and C$_0$=[4-NP]$_{t=0}$ deduced from the maximum of absorbance, evolves linearly with time (t) (Figure 8). From the slop of the lines, we deduced the apparent rate constants (K_{app}) (see table SI.17) of the reaction for Ag, A@Pt and Pt nanocatalysts. Monometallic Pt NPs showed a 24% increase in K_{app} compared to that of Ag NPs while the K_{app} for Ag@Pt$_{1.1nm}$ remains larger with a 50% increase compared to Pt NPs. These results highlight the synergistic catalytic effect of Ag and Pt species, which may be due to several effects.

First, this effect may stem from the electronic structure of Ag@Pt core-shell NPs. DFT calculations have shown that in Ag@Pt core-shell NPs, electrons accumulate in the Pt region, and Pt atomic population become more negatively charged compared to Ag core subsequent to Pt coating, indicating a charge transfer from Ag to Pt layers.[55] This is associated with a strong (Ag)s-(Pt)d hybridization at the origin of the charge redistribution between Ag cores and Pt shells. The increased electron density in the Pt layer makes more electrons available for the NP reduction at the surface and may be responsible of the improved catalytic performance of Ag@Pt compared to pure Ag and Pt NPs. Secondly, the LSPRs of Ag NPs are excited during the recording of the in-situ UV-visible spectra performed in this study (see Figure SI.18). We did not observe the NP LSPR since concentration are extremely low, and the absorbance is dominated by 4-NP in the same spectral range at 400nm. In plasmonic catalysis, light can improve catalytic reaction by several process namely enhanced EM fields (plasmonic antenna), plasmonic heating effect and hot electron generation.[56,57] The latter two are related to the LSPR excitation and the former to the increase of photon flux at the NP due to the focusing of the electromagnetic field by the plasmonic antenna. Each of the effect show potential to contribute to the catalytic reaction of 4-NP reduction. The local photo-induced heating around an individual NP in a diluted solution under irradiation can be estimated [56] and is very low (around 3 mK) (see details in SI.19). This calculation is strictly valid for non-thermodynamically interacting plasmonic NPs, as thermodynamic coupling could produce much larger temperature variation.[58] Here the concentration in our solution is so low that we can safely assume that the NPs can be considered as non-thermodynamically interacting. Therefore, we cannot attribute the increase in reactivity observed with Ag@Pt NPs to local heating due to Ag absorption. The role of hot electrons can be also excluded as the Pt shell thickness is too high [59]. Only antenna effect can be considered in our case, as it was demonstrated that enhanced EM fields can indeed promote the adsorptions of reactants on the NPs surface according to the literature [57,60] and thus the charge transfer mechanism for the reduction of 4-NP into 4-AP. Ag@Pt NPs appears thus as promising candidate for catalysis owing to their intrinsic catalytic activity and to the LSPR of Ag core. Further experiments have to be carried out for the maximum utilization of these core-shell NPs with tunable composition and size.

3. Conclusion

Ag@Pt core-shell NPs were successfully synthesized with controlled size, size dispersion and chemical composition through a versatile approach using Ag seeds with selected sizes. Seed size control was obtained by vaying the reaction temperature and using a selected ramping rate. The final Pt thickness of the core-shell NPs was shown to depend on the [shell precursor]/ [metal seeds] concentration ratio for an optimum reaction temperature of 200°C and a reaction time of 1 hour. The core-shell structure was confirmed by EELS maps and UV-visible spectroscopy coupled with DDA calculations. Finally, this protocol was extended to other plasmonic and catalytic bimetallic systems. Bimetallic core-shell Ag@Pd and Au@Pt NPs with controlled composition were synthesized without strong modification of the synthesis process. The shell growth was still controlled by [metallic precursor]/[seed] concentration ratio. The plasmonic properties of the $Ag_{8.4nm}$@Pt NPs were studied as a function of the Pt shell thickness by UV-vis absorption spectroscopy and DDA calculations. We obtained a critical Pt shell thickness of 1.1 nm (4 atomic layers) above which the Ag core LSPR is completely damped.

We have also demonstrated that the Ag@$Pt_{1.1nm}$ NPs were catalytically active in the conversion of 4-NP to 4-AP in the presence of $NaBH_4$. In addition, these NPs present a higher activity than monometallic Ag and Pt NPs with similar sizes. These results therefore highlight the synergistic catalytic effect of Ag and Pt species which may be due to the electronic structure of Ag@Pt core-shell NPs, but which may also benefit from the LSPR excitation of the Ag core. Further work is therefore underway to study the plasmonic catalytic activity of these core-shell NPs as a function of their composition and size. The high quality of the samples and the high degree of control of the core and shell parameters will be of great interest for these future studies, and should help to disentangle the different mechanisms involved in plasmonic catalysis.

ASSOCIATED CONTENT

Supporting Information. The following files are available free of charge. Additional figures illustrating the synthesis of AgNPs and Ag@Pt NPs with the evolution of the reaction conditions (ramping rates and temperatures), the characterization of the NPs (TEM images, size distributions and UV-vis spectra), the detail of the Pt thickness calculation from the TEM images, the ligand exchange process and characterization and finally additional data concerning the catalytic performance of Ag@Pt Pps for the reduction of 4NP into 4AP.

AUTHOR INFORMATION

Corresponding Author

*Pr Alexa Courty: alexa.courty@sorbonne-universite.fr; * Dr Caroline Salzmann: caroline.salzemann@sorbonne-universite.fr ;

Author Contribution

The manuscript was written through contributions of all authors. All authors have given approval to the final version of the manuscript**.**

ACKNOWLEDGMENT

The authors thank the Chinese Scholarship Council for the thesis grant. AC, CS and AG thank Sorbonne University and the CNRS for facilities. MW thanks the EU ESTEEM3 grant agreement (No 823717) and the French METSA network (FR CNRS 3507).

References

(1) Che, M.; Bennett, C. O. The Influence of Particle Size on the Catalytic Properties of Supported Metals. In *Advances in Catalysis*; Elsevier, 1989; Vol. 36, pp 55–172. https://doi.org/10.1016/S0360-0564(08)60017-6.

(2) Haruta, M. Size- and Support-Dependency in the Catalysis of Gold. *Catalysis Today* **1997**, *36* (1), 153–166. https://doi.org/10.1016/S0920-5861(96)00208-8.

(3) A. Bhosale, M.; M. Bhanage, B. Silver Nanoparticles: Synthesis, Characterization and Their Application as a Sustainable Catalyst for Organic Transformations. *Current Organic Chemistry* **2015**, *19* (8), 708–727. https://doi.org/10.2174/1385272819666150207001154.

(4) Dong, X.-Y.; Gao, Z.-W.; Yang, K.-F.; Zhang, W.-Q.; Xu, L.-W. Nanosilver as a New Generation of Silver Catalysts in Organic Transformations for Efficient Synthesis of Fine Chemicals. *Catalysis Science & Technology* **2015**, *5* (5), 2554–2574. https://doi.org/10.1039/C5CY00285K.

(5) Christopher, P.; Xin, H.; Linic, S. Visible-Light-Enhanced Catalytic Oxidation Reactions on Plasmonic Silver Nanostructures. *Nature Chemistry* **2011**, *3* (6), 467–472. https://doi.org/10.1038/nchem.1032.

(6) Mukherjee, S.; Libisch, F.; Large, N.; Neumann, O.; Brown, L. V.; Cheng, J.; Lassiter, J. B.; Carter, E. A.; Nordlander, P.; Halas, N. J. Hot Electrons Do the Impossible: Plasmon-Induced Dissociation of H_2 on Au. *Nano Lett.* **2013**, *13* (1), 240–247. https://doi.org/10.1021/nl303940z.

(7) Gargiulo, J.; Berté, R.; Li, Y.; Maier, S. A.; Cortés, E. From Optical to Chemical Hot Spots in Plasmonics. *Acc. Chem. Res.* **2019**, *52* (9), 2525–2535. https://doi.org/10.1021/acs.accounts.9b00234.

(8) Liu, T.; Besteiro, L. V.; Liedl, T.; Correa-Duarte, M. A.; Wang, Z.; Govorov, A. O. Chiral Plasmonic Nanocrystals for Generation of Hot Electrons: Toward Polarization-Sensitive Photochemistry. *Nano Lett.* **2019**, *19* (2), 1395–1407. https://doi.org/10.1021/acs.nanolett.8b05179.

(9) Gellé, A.; Jin, T.; de la Garza, L.; Price, G. D.; Besteiro, L. V.; Moores, A. Applications of Plasmon-Enhanced Nanocatalysis to Organic Transformations. *Chem. Rev.* **2020**, *120* (2), 986–1041. https://doi.org/10.1021/acs.chemrev.9b00187.

(10) Li, S.; Miao, P.; Zhang, Y.; Wu, J.; Zhang, B.; Du, Y.; Han, X.; Sun, J.; Xu, P. Recent Advances in Plasmonic Nanostructures for Enhanced Photocatalysis and Electrocatalysis. *Adv. Mater.* **2021**, *33* (6), 2000086. https://doi.org/10.1002/adma.202000086.

(11) Mao, C.; Li, H.; Gu, H.; Wang, J.; Zou, Y.; Qi, G.; Xu, J.; Deng, F.; Shen, W.; Li, J.; Liu, S.; Zhao, J.; Zhang, L. Beyond the Thermal Equilibrium Limit of Ammonia Synthesis with Dual Temperature Zone Catalyst Powered by Solar Light. *Chem* **2019**, *5* (10), 2702–2717. https://doi.org/10.1016/j.chempr.2019.07.021.

(12) Favier, I.; Pla, D.; Gómez, M. Palladium Nanoparticles in Polyols: Synthesis, Catalytic Couplings, and Hydrogenations. *Chem. Rev.* **2020**, *120* (2), 1146–1183. https://doi.org/10.1021/acs.chemrev.9b00204.

(13) Heuer-Jungemann, A.; Feliu, N.; Bakaimi, I.; Hamaly, M.; Alkilany, A.; Chakraborty, I.; Masood, A.; Casula, M. F.; Kostopoulou, A.; Oh, E.; Susumu, K.; Stewart, M. H.; Medintz, I. L.; Stratakis, E.; Parak, W. J.; Kanaras, A. G. The Role of Ligands in the Chemical Synthesis and Applications of Inorganic Nanoparticles. *Chemical Reviews* **2019**, *119* (8), 4819–4880. https://doi.org/10.1021/acs.chemrev.8b00733.

(14) Jin, R.; Zeng, C.; Zhou, M.; Chen, Y. Atomically Precise Colloidal Metal Nanoclusters and

Nanoparticles: Fundamentals and Opportunities. *Chem. Rev.* **2016**, *116* (18), 10346–10413. https://doi.org/10.1021/acs.chemrev.5b00703.

(15) Liu, L.; Corma, A. Metal Catalysts for Heterogeneous Catalysis: From Single Atoms to Nanoclusters and Nanoparticles. *Chem. Rev.* **2018**, *118* (10), 4981–5079. https://doi.org/10.1021/acs.chemrev.7b00776.

(16) Liu, D.; Yang, N.; Zeng, Q.; Liu, H.; Chen, D.; Cui, P.; Xu, L.; Hu, C.; Yang, J. Core-Shell Ag–Pt Nanoparticles: A Versatile Platform for the Synthesis of Heterogeneous Nanostructures towards Catalyzing Electrochemical Reactions. *Chinese Chemical Letters* **2021**, *32* (11), 3288–3297. https://doi.org/10.1016/j.cclet.2021.04.053.

(17) Xu, D.; Xu, P.; Wang, X.; Chen, Y.; Yu, H.; Zheng, D.; Li, X. Pentagram-Shaped Ag@Pt Core–Shell Nanostructures as High-Performance Catalysts for Formaldehyde Detection. *ACS Appl. Mater. Interfaces* **2020**, *12* (7), 8091–8097. https://doi.org/10.1021/acsami.9b17201.

(18) Alayoglu, S.; Nilekar, A. U.; Mavrikakis, M.; Eichhorn, B. Ru–Pt Core–Shell Nanoparticles for Preferential Oxidation of Carbon Monoxide in Hydrogen. *Nature Mater* **2008**, *7* (4), 333–338. https://doi.org/10.1038/nmat2156.

(19) Ferrando, R.; Jellinek, J.; Johnston, R. L. Nanoalloys: From Theory to Applications of Alloy Clusters and Nanoparticles. *Chem. Rev.* **2008**, *108* (3), 845–910. https://doi.org/10.1021/cr040090g.

(20) *Bimetallic Nanostructures: Shape-Controlled Synthesis for Catalysis, Plasmonics, and Sensing Applications*; Zhang, Y.-W., Ed.; John Wiley & Sons: Hoboken, NJ, 2018.

(21) Han, G.-H.; Kim, K. Y.; Nam, H.; Kim, H.; Yoon, J.; Lee, J.-H.; Kim, H.-K.; Ahn, J.-P.; Lee, S. Y.; Lee, K.-Y.; Yu, T. Facile Direct Seed-Mediated Growth of AuPt Bimetallic Shell on the Surface of Pd Nanocubes and Application for Direct H2O2 Synthesis. *Catalysts* **2020**, *10* (6), 650. https://doi.org/10.3390/catal10060650.

(22) Bhol, P.; Bhavya, M. B.; Swain, S.; Saxena, M.; Samal, A. K. Modern Chemical Routes for the Controlled Synthesis of Anisotropic Bimetallic Nanostructures and Their Application in Catalysis. *Front Chem* **2020**, *8*, 357. https://doi.org/10.3389/fchem.2020.00357.

(23) Rodríguez, R. C.; Troiani, H.; Moya, S. E.; Bruno, M. M.; Angelomé, P. C. Bimetallic Ag-Au Nanoparticles Inside Mesoporous Titania Thin Films: Synthesis by Photoreduction and Galvanic Replacement, and Catalytic Activity. *Eur. J. Inorg. Chem.* **2020**, *2020* (6), 568–574. https://doi.org/10.1002/ejic.201901186.

(24) da Silva, A. G. M.; Rodrigues, T. S.; Haigh, S. J.; Camargo, P. H. C. Galvanic Replacement Reaction: Recent Developments for Engineering Metal Nanostructures towards Catalytic Applications. *Chem. Commun.* **2017**, *53* (53), 7135–7148. https://doi.org/10.1039/C7CC02352A.

(25) Moumen, A.; Halim, W.; Jaffal, S.; Abderrafi, K.; Eddahbi, A.; Sebti, S.; Ouaskit, S. Microwave Assisted Synthesis of Palladium Nanoparticles in an Aqueous Emulsion of Copolymer: Application to Catalysis. *J Clust Sci* **2017**, *28* (5), 2817–2832. https://doi.org/10.1007/s10876-017-1259-0.

(26) Liu, A.; Liu, X.; Liu, L.; Pu, Y.; Guo, K.; Tan, W.; Gao, S.; Luo, Y.; Yu, S.; Si, R.; Shan, B.; Gao, F.; Dong, L. Getting Insights into the Temperature-Specific Active Sites on Platinum Nanoparticles for CO Oxidation: A Combined in Situ Spectroscopic and Ab Initio Density Functional Theory Study. *ACS Catal.* **2019**, *9* (9), 7759–7768. https://doi.org/10.1021/acscatal.9b02552.

(27) Lee, S.; Portalès, H.; Walls, M.; Beaunier, P.; Goubet, N.; Tremblay, B.; Margueritat, J.; Saviot, L.; Courty, alexa. Versatile and Robust Synthesis Process for the Fine Control of the

Chemical Composition and Core-Crystallinity of Spherical Core-Shell Au@Ag Nanoparticles. *Nanotechnology* **2020**. https://doi.org/10.1088/1361-6528/abc450.

(28) Andrieux-Ledier, A.; Tremblay, B.; Courty, A. Synthesis of Silver Nanoparticles Using Different Silver Phosphine Precursors: Formation Mechanism and Size Control. *The Journal of Physical Chemistry C* **2013**, *117* (28), 14850–14857. https://doi.org/10.1021/jp4040248.

(29) Wei, J. J.; Yang, P.; Portalès, H.; Albouy, P.-A.; Pileni, M. P. Collective Surface Plasmon Resonances in Two-Dimensional Assemblies of Au and Ag Nanocrystals: Experiments and Discrete Dipole Approximation Simulation. *The Journal of Physical Chemistry C* **2016**, *120* (25), 13732–13738. https://doi.org/10.1021/acs.jpcc.6b03397.

(30) Draine, B. T.; Flatau, P. J. Discrete-Dipole Approximation For Scattering Calculations. *Journal of the Optical Society of America A* **1994**, *11* (4), 1491. https://doi.org/10.1364/JOSAA.11.001491.

(31) Draine, B. T.; Flatau, P. J. User Guide for the Discrete Dipole Approximation Code DDSCAT 7.3. *arXiv:1305.6497 [astro-ph, physics:cond-mat, physics:physics]* **2013**.

(32) *Handbook of Optical Constants of Solids*, 6. Nachdr.; Palik, E. D., Ed.; Acad. Press: Boston, 2004.

(33) Gilroy, K. D.; Ruditskiy, A.; Peng, H.-C.; Qin, D.; Xia, Y. Bimetallic Nanocrystals: Syntheses, Properties, and Applications. *Chem. Rev.* **2016**, *116* (18), 10414–10472. https://doi.org/10.1021/acs.chemrev.6b00211.

(34) Hou, P.; Liu, H.; Li, J.; Yang, J. One-Pot Synthesis of Noble Metal Nanoparticles with a Core–Shell Construction. *CrystEngComm* **2015**, *17* (8), 1826–1832. https://doi.org/10.1039/C4CE02560A.

(35) Calvo, F. Thermodynamics of Nanoalloys. *Physical Chemistry Chemical Physics* **2015**, *17* (42), 27922–27939. https://doi.org/10.1039/C5CP00274E.

(36) Prasad, B. L. V.; Stoeva, S. I.; Sorensen, C. M.; Klabunde, K. J. Digestive Ripening of Thiolated Gold Nanoparticles: The Effect of Alkyl Chain Length. *Langmuir* **2002**, *18* (20), 7515–7520. https://doi.org/10.1021/la020181d.

(37) Shimpi, J. R.; Sidhaye, D. S.; Prasad, B. L. V. Digestive Ripening: A Fine Chemical Machining Process on the Nanoscale. *Langmuir* **2017**, *33* (38), 9491–9507. https://doi.org/10.1021/acs.langmuir.7b00193.

(38) Horvath, H. Gustav Mie and the Scattering and Absorption of Light by Particles: Historic Developments and Basics. *Journal of Quantitative Spectroscopy and Radiative Transfer* **2009**, *110* (11), 787–799. https://doi.org/10.1016/j.jqsrt.2009.02.022.

(39) Peng, S.; McMahon, J. M.; Schatz, G. C.; Gray, S. K.; Sun, Y. Reversing the Size-Dependence of Surface Plasmon Resonances. *Proceedings of the National Academy of Sciences* **2010**, *107* (33), 14530–14534. https://doi.org/10.1073/pnas.1007524107.

(40) Campos, A.; Troc, N.; Cottancin, E.; Pellarin, M.; Weissker, H.-C.; Lermé, J.; Kociak, M.; Hillenkamp, M. Plasmonic Quantum Size Effects in Silver Nanoparticles Are Dominated by Interfaces and Local Environments. *Nat. Phys.* **2019**, *15* (3), 275–280. https://doi.org/10.1038/s41567-018-0345-z.

(41) Cobley, C. M.; Xia, Y. Engineering the Properties of Metal Nanostructures via Galvanic Replacement Reactions. *Mater Sci Eng R Rep* **2010**, *70* (3–6), 44–62.

https://doi.org/10.1016/j.mser.2010.06.002.

(42) Mourdikoudis, S.; Liz-Marzán, L. M. Oleylamine in Nanoparticle Synthesis. *Chem. Mater.* **2013**, *25* (9), 1465–1476. https://doi.org/10.1021/cm4000476.

(43) Yin, X. Effects of Metal Ion–Ligand Interactions on the Synthesis of Metal Nanostructures with Controlled Morphology. **2015**. https://doi.org/10.13140/RG.2.2.32232.72960.

(44) Xia, Y.; Gilroy, K. D.; Peng, H.-C.; Xia, X. Seed-Mediated Growth of Colloidal Metal Nanocrystals. *Angew. Chem. Int. Ed.* **2017**, *56* (1), 60–95. https://doi.org/10.1002/anie.201604731.

(45) Zhao, X.; Zhang, J.; Wang, B.; Zada, A.; Humayun, M. Biochemical Synthesis of Ag/AgCl Nanoparticles for Visible-Light-Driven Photocatalytic Removal of Colored Dyes. *Materials (Basel)* **2015**, *8* (5), 2043–2053. https://doi.org/10.3390/ma8052043.

(46) Chee, S. W.; Tan, S. F.; Baraissov, Z.; Bosman, M.; Mirsaidov, U. Direct Observation of the Nanoscale Kirkendall Effect during Galvanic Replacement Reactions. *Nat Commun* **2017**, *8* (1), 1224. https://doi.org/10.1038/s41467-017-01175-2.

(47) Chapus, L.; Aubertin, P.; Joiret, S.; Lucas, I. T.; Maisonhaute, E.; Courty, A. Tunable SERS Platforms from Small Nanoparticle 3D Superlattices: A Comparison between Gold, Silver, and Copper. *ChemPhysChem* **2017**, *18* (21), 3066–3075. https://doi.org/10.1002/cphc.201700601.

(48) Zaleska-Medynska, A.; Marchelek, M.; Diak, M.; Grabowska, E. Noble Metal-Based Bimetallic Nanoparticles: The Effect of the Structure on the Optical, Catalytic and Photocatalytic Properties. *Advances in Colloid and Interface Science* **2016**, *229*, 80–107. https://doi.org/10.1016/j.cis.2015.12.008.

(49) Kuroda, K.; Ishida, T.; Haruta, M. Reduction of 4-Nitrophenol to 4-Aminophenol over Au Nanoparticles Deposited on PMMA. *Journal of Molecular Catalysis A: Chemical* **2009**, *298* (1–2), 7–11. https://doi.org/10.1016/j.molcata.2008.09.009.

(50) Noh, J.-H.; Meijboom, R. Synthesis and Catalytic Evaluation of Dendrimer-Templated and Reverse Microemulsion Pd and Pt Nanoparticles in the Reduction of 4-Nitrophenol: The Effect of Size and Synthetic Methodologies. *Applied Catalysis A: General* **2015**, *497*, 107–120. https://doi.org/10.1016/j.apcata.2015.02.039.

(51) Wang, Z.; Xu, C.; Gao, G.; Li, X. Facile Synthesis of Well-Dispersed Pd–Graphene Nanohybrids and Their Catalytic Properties in 4-Nitrophenol Reduction. *RSC Adv.* **2014**, *4* (26), 13644. https://doi.org/10.1039/c3ra47721e.

(52) Dabera, G. D. M. R.; Walker, M.; Sanchez, A. M.; Pereira, H. J.; Beanland, R.; Hatton, R. A. Retarding Oxidation of Copper Nanoparticles without Electrical Isolation and the Size Dependence of Work Function. *Nat Commun* **2017**, *8* (1), 1894. https://doi.org/10.1038/s41467-017-01735-6.

(53) Yang, Y.; Serrano, L. A.; Guldin, S. A Versatile AuNP Synthetic Platform for Decoupled Control of Size and Surface Composition. *Langmuir* **2018**, *34* (23), 6820–6826. https://doi.org/10.1021/acs.langmuir.8b00353.

(54) Salgueiriño-Maceira, V.; Liz-Marzán, L. M.; Farle, M. Water-Based Ferrofluids from Fe $_{x}$ Pt $_{1-x}$ Nanoparticles Synthesized in Organic Media. *Langmuir* **2004**, *20* (16), 6946–6950. https://doi.org/10.1021/la049300a.

(55) Ma, Y.; Wu, X.; Zhang, G. Core-Shell Ag@Pt Nanoparticles Supported on Sepiolite Nanofibers for the Catalytic Reduction of Nitrophenols in Water: Enhanced Catalytic Performance and DFT Study. *Applied Catalysis B: Environmental* **2017**, *205*, 262–270.

https://doi.org/10.1016/j.apcatb.2016.12.025.

(56) Baffou, G.; Quidant, R. Nanoplasmonics for Chemistry. *Chem. Soc. Rev.* **2014**, *43* (11), 3898. https://doi.org/10.1039/c3cs60364d.

(57) Xin, Y.; Yu, K.; Zhang, L.; Yang, Y.; Yuan, H.; Li, H.; Wang, L.; Zeng, J. Copper-Based Plasmonic Catalysis: Recent Advances and Future Perspectives. *Advanced Materials* **2021**, *33* (32), 2008145. https://doi.org/10.1002/adma.202008145.

(58) Baffou, G.; Berto, P.; Bermúdez Ureña, E.; Quidant, R.; Monneret, S.; Polleux, J.; Rigneault, H. Photoinduced Heating of Nanoparticle Arrays. *ACS Nano* **2013**, *7* (8), 6478–6488. https://doi.org/10.1021/nn401924n.

(59) Zhang, H.; Wei, J.; Zhang, X.-G.; Zhang, Y.-J.; Radjenovica, P. M.; Wu, D.-Y.; Pan, F.; Tian, Z.-Q.; Li, J.-F. Plasmon-Induced Interfacial Hot-Electron Transfer Directly Probed by Raman Spectroscopy. *Chem* **2020**, *6* (3), 689–702. https://doi.org/10.1016/j.chempr.2019.12.015.

(60) Mori, K.; Kawashima, M.; Che, M.; Yamashita, H. Enhancement of the Photoinduced Oxidation Activity of a Ruthenium(II) Complex Anchored on Silica-Coated Silver Nanoparticles by Localized Surface Plasmon Resonance. *Angewandte Chemie International Edition* **2010**, *49* (46), 8598–8601. https://doi.org/10.1002/anie.201004942.

SYNOPSIS

EELS mapping and in-situ UV-visible spectra for monitoring the catalytic activity of Ag@Pt NPs via the model reaction of reduction of 4-NP into 4-AP